J. Fluid Mech. (2001), *vol.* 442, *pp.* 217–239. Printed in the United Kingdom

Evaporative instabilities in climbing films

By A. E. HOSOI AND JOHN W. M. BUSH

Department of Mathematics, Massachusetts Institute of Technology, 77 Massachusetts Avenue, Cambridge, MA 02139, USA

(Received 5 April 2000 and in revised form 12 February 2001)

We consider flow in a thin film generated by partially submerging an inclined rigid plate in a reservoir of ethanol– or methanol–water solution and wetting its surface. Evaporation leads to concentration and surface tension gradients that drive flow up the plate. An experimental study indicates that the climbing film is subject to two distinct instabilities. The first is a convective instability characterized by flattened convection rolls aligned in the direction of flow and accompanied by free-surface deformations; in the meniscus region, this instability gives rise to pronounced ridge structures aligned with the mean flow. The second instability, evident when the plate is nearly vertical, takes the form of transverse surface waves propagating up the plate.

We demonstrate that the observed longitudinal rolls are driven by the combined influence of surface deformations and alcohol concentration gradients. Guided by the observation that the rolls are flattened, we develop a quasi-two-dimensional theoretical model for the instability of the film, based on lubrication theory, which includes the effects of gravity, capillarity and Marangoni stresses at the surface. We develop stability criteria for the film which are in qualitative agreement with our experimental observations. Our analysis yields an equation for the shape of the interface which is solved numerically and reproduces the salient features of the observed flows, including the slow lateral drift and merging of the ridges.

1. Introduction

The study of evaporatively driven convection has a rich history dating back to 1855 when Thomson reported 'On certain curious Motions observable at the Surfaces of Wine and other Alcoholic Liquors'. Thomson correctly attributed these convective motions to stresses at the free surface of the fluid associated with variations in surface tension resulting from evaporatively driven gradients in alcohol concentration. In a wine glass, evaporation results in relatively low alcohol concentration and thus high surface tension in the thin film above the meniscus. The wine is drawn up the walls of the glass and accumulates in a thick band at the upper edge of the film until the band becomes unstable and releases the 'tears of wine.' After Thomson's treatise, Marangoni (1865) inferred that convection could be driven by surface tension gradients due to variations in either composition or temperature and today this mode of convection bears his name (see historical reviews by Scriven & Sternling 1960; Ross & Becher 1992).

Evaporative convection arises in a variety of natural and industrial settings, and an extensive review of its manifestations may be found in Berg, Acrivos & Boudart (1966). Evaporation from the free surface of a homogeneous fluid leads to surface cooling, and so may drive one of two forms of instability: Marangoni convection, which

relies on the temperature dependence of the surface tension, or Rayleigh–Bénard convection which relies explicitly on the generation of buoyancy through the influence of temperature on the fluid density. In a multicomponent system, such as alcohol and water, evaporation of the volatile component also leads to gradients in chemical composition which may further destabilize the system to 'chemical' or 'compositional' convection which may analogously take either Marangoni or Rayleigh–Bénard forms.

Bénard's (1900) seminal experimental observations of cellular convection in a horizontal layer of spermaceti heated from below were originally erroneously attributed to buoyancy-driven thermal convection (Rayleigh 1916), but are now known to have been due to Marangoni effects (Block 1956; Koschmieder 1967). Pearson (1958) examined the stability of a horizontal layer of depth H of fluid of viscosity μ, density ρ and thermal diffusivity κ, driven by a vertical temperature gradient, $\Theta \equiv \mathrm{d}T/\mathrm{d}z$, with a non-deformable interface, in which surface tension is a monotonically decreasing function of temperature, $\mathrm{d}\sigma/\mathrm{d}T \equiv -\gamma$. If the surface temperature is increased locally, the resulting surface tension gradient will drive surface divergence and draw warm fluid up from below. If the timescale of thermal diffusion of the upwelling fluid, H^2/κ, exceeds the convective timescale, μ/τ, where $\tau = \gamma\Theta$ is the characteristic surface stress, then the upwelling fluid retains its heat, the surface perturbation is enhanced and Marangoni convection is sustained. Pearson (1958) deduced the criterion for convective instability in terms of the Marangoni number: $M = \gamma\Theta H^2/\mu\kappa > 80$. Nield (1964) extended Pearson's analysis through considering the combined influence of surface tension effects and buoyancy on a fluid layer heated from below, and found that the critical Marangoni number is decreased by the influence of fluid buoyancy. Since the Marangoni number increases with H^2 while the Rayleigh number, $Ra = \rho g\beta\Theta H^4/\kappa\mu$ (where g is acceleration due to gravity and β is the coefficient of thermal expansion) increases with H^3 (since $\Theta \sim H^{-1}$), the relative importance of Rayleigh–Bénard and Marangoni convection decreases with decreasing layer depth: Marangoni convection can operate in fluid layers which are too thin to support Rayleigh–Bénard convection.

Scriven & Sternling (1964) extended Pearson's analysis to include a deformable interface and demonstrated that this added degree of freedom renders the system convectively unstable at all Marangoni numbers. The authors also pointed out a useful qualitative distinction between Marangoni and Rayleigh–Bénard convection: under elevations in the free surface, the former is characterized by downwelling and the latter by upwelling. Smith (1966) demonstrated that the destabilizing influence of the deformable free surface may be mitigated by the influence of gravity, and his stability criterion may be expressed as $\gamma\Theta < \frac{2}{3}\rho gH$; consequently, long-wave instabilities always become important in sufficiently thin films (Davis 1987). These previous analyses are summarized in table 1.

An exploratory experimental study of evaporatively forced convection within layers of both homogeneous and binary fluids was presented by Berg, Boudart & Acrivos (1966), who observed a variety of flow structures, including hexagonal cellular patterns reminiscent of Bénard's original experiments, and pronounced linear features, termed 'streamers' and 'ribs', which correspond to regions of vigorous convective upwelling or downwelling. The effect of nonlinear temperature profiles, as may arise through evaporation from a free surface, on the onset of Marangoni convection was examined by Vidal & Acrivos (1968), who demonstrated that fluid layers are more convectively stable if they have nonlinear rather than linear temperature profiles. The linear instability of a horizontal fluid layer destabilized by evaporation from a flat free surface has been considered by Yang (1999). A recent experimental study of evaporatively induced convection in free or thermally forced fluid layers is that by

		Quiescent layer heated from below	Sheared layer
Flat interface	$g = 0$	Pearson (1958)	Smith & Davis (1983*a*)
	$g \neq 0$	Nield (1964)	—
Deformable interface	$g = 0$	Scriven & Sternling (1964)	Smith & Davis (1983*b*)*
	$g \neq 0$	Smith (1966)	Present Study

TABLE 1. A summary of previous analyses of the stability of fluid layers under the influence of Marangoni forcing. $g \neq 0$ means gravitational effects were included in the analysis. *Here Smith & Davis consider surface deformations associated with transverse waves not longitudinal rolls.

Chai & Zhang (1998), who propose a modified Marangoni number appropriate for describing the stability of evaporating fluid layers.

Smith & Davis (1983*a*, *b*) examined the convective stability of horizontal shear flows in zero gravity. The presence of a lateral temperature gradient leads to a surface stress that drives a shear flow, and the resulting vertical temperature profile is capable of destabilizing the layer to Marangoni convection. Both the critical Marangoni number and the form of instability at onset were found to depend on the Prandtl number. In the limit of low Prandtl number, the layer is most unstable to hydrothermal waves propagating in, and aligned perpendicular to, the direction of the applied stress (Smith & Davis 1983*b*). In the limit of large Prandtl number, the layer is most unstable to flattened convection rolls aligned with the flow (Smith & Davis 1983*a*). For linear flow profiles and Prandtl numbers of order 1000, the fluid layer becomes unstable to steady convection rolls with a wavelength approximately ten times the layer depth. Their study was motivated by two particular applications in which the deformation of the free surface was unimportant; consequently, they did not examine the potentially destabilizing influence of this added degree of freedom. Motivated by our observations of longitudinal convection rolls and accompanying free-surface deformations in an inclined evaporating shear layer, we extend the theoretical model of Smith & Davis (1983*a*) through inclusion of the combined influence of gravity and a deformable free surface.

Our current study was originally motivated by the free-surface instability reported by Fournier & Cazabat (1992) to exist in the meniscus region in glasses of strong wine exhibiting the 'tears of wine' phenomenon. The instability assumes the form of ridges aligned perpendicular to the meniscus, as illustrated in figure 1. In a wine glass, the structures appear from above as a radial spoke pattern around the meniscus, and so were referred to by the authors as the 'star-instability'. The phenomenon was subsequently examined experimentally by Vuilleumier *et al.* (1995) and Fanton & Cazabat (1998). Owing to the thinness of the film (20–100 μm), Cazabat and coworkers were unable to observe convection within the film, and so were led to hypothesize that the ridges are a surface manifestation of a Rayleigh–Plateau instability driven by competing curvatures in the free surface of the meniscus. Prompted by these observations and this conjecture, de Ryck (1999) formulated a theoretical model which neglected the influence of convection in the thin film. In this study, we re-examine the system experimentally and clearly demonstrate the presence of vigorous evaporative convection within the film. Moreover, we demonstrate that the ridges are the dynamically sustained surface manifestation of streamwise Marangoni convection rolls.

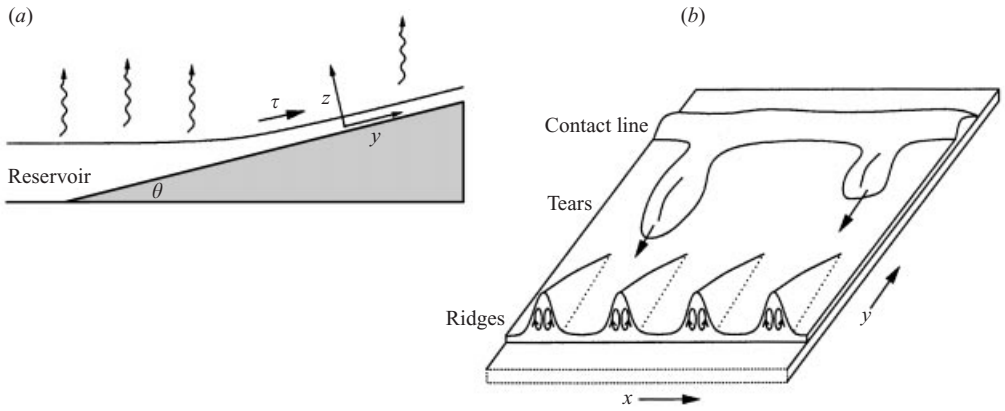

FIGURE 1. Schematic of the system. The ridges and tears in (*b*) are not drawn to scale. Arrows in the ridges illustrate the two counter-rotating convection cells within each ridge.

The influence of thermally induced surface tension gradients on thin films has been investigated using lubrication theory, and three comprehensive reviews of these studies are presented by Davis (1987), Oron, Davis & Bankoff (1997) and Myers (1998). Of particular interest to our study is that of Burelbach, Bankoff & Davis (1988), who considered the influence of evaporation on the evolution of thin films. It is important to note that the lubrication description permits only unidirectional flow within films constrained by a stress-free surface condition, but permits convection rolls within films forced by non-uniform surface stresses. This is particularly evident in the study of Oron & Rosenau (1994) who examined the influence of a quadratic temperature dependence of surface tension on the evolution of a thin film heated from below. Here we develop a theoretical framework for describing the flattened convection rolls observed in our film based on a lubrication approximation.

In § 2, we present the results of an experimental study of the fluid motions observed when an inclined plate is partially submerged in a reservoir of evaporating fluid. We describe the form of the instabilities and their dependence on the governing parameters. In § 3, we provide a qualitative description of the physical mechanisms responsible for the observed instabilities. In § 4, we develop a mathematical model describing the observed instabilities, and deduce stability criteria for the film. The model is based on a lubrication approximation, and results in a fourth-order partial differential equation for the interface shape which is solved numerically in § 5. In § 6, we summarize the experiments and theoretical model, and discuss the broader relevance of our study.

2. Experiments

Methanol– and ethanol–water solutions were poured into a shallow rectangular vessel and a glass plate was partially submerged at an inclination angle θ relative to the horizontal (figure 1). The plate was wet up to several centimetres above the free surface of the reservoir. The transient phase which follows is noteworthy. Seconds after the wetting of the glass, an oblong shallow patch forms directly above the meniscus. The lower edge of the oblong indentation remains fixed on the meniscus, while the upper edge is swept upwards at approximately $1\,\mathrm{mm\,s^{-1}}$ in the form of a front between thin and thick films (figure 2*a*). The oblong indentation expands until

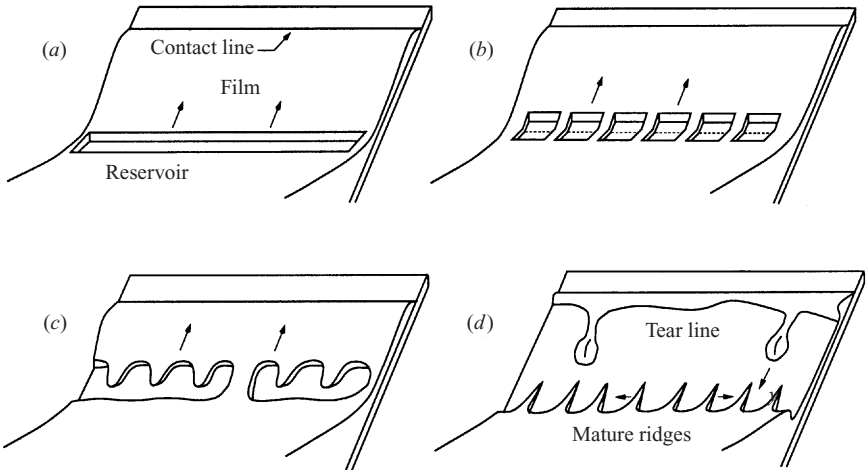

FIGURE 2. Schematic of the transient phase which follows the initial wetting of the plate.

it becomes unstable and breaks into a series of regular indentations which are divided by the first observable ridges (figure 2*b*). These ridges are initially marked by relatively vigorous upflow, but then typically grow in amplitude and broaden until the upflow ceases and the ridges slump back towards the reservoir (figure 2*c*). Subsequently, new ridge structures form throughout the meniscus region, and drift laterally in either direction with a characteristic speed of $1\,\mathrm{mm\,s^{-1}}$ leading to occasional ridge merger (figure 2*d*). The spacing of the ridges after the breakup of the oblong indentation is approximately equal to the length of the indentation, and decreases with angle of plate inclination. However, the subsequent emergence of ridges is more irregular and their motion suggests that the ridges are not simply a relic of an instability of the developing meniscus, but are rather a surface signature of the dynamics in the thin film.

Approximately 10–20 s after the initial wetting of the plate, a quasi-steady state was established (figure 2*d*). This state was characterized by ridges meandering, merging and re-forming and being occasionally disrupted by falling tears. The surface deformations were visualized using a shadowgraph. By sprinkling Lycopodium powder on the free surface, it was possible to trace the surface flow, which revealed the ridges as focal points of upflow in the meniscus region. Figure 3 is a photograph in which the three-dimensionality of the tears and ridges is clearly evident.

Owing to the thinness of the film, convective motions could not be exposed with traditional dye techniques, but were revealed by adding to the solution small amounts of Kalliroscope, which is composed of micron scale platelets (derived from fish scales) that align with shear. The Kalliroscope revealed a wealth of convective patterns within the flow, including large-scale polygonal convection patterns within the reservoir, and finer linear features within the film (figure 4). The crest of each ridge was marked by a dark line corresponding to a line of surface convergence separating two convection cells which together comprise the ridge (figure 4). The Kalliroscope also revealed much finer ($< 0.5\,\mathrm{mm}$ scale) convective motions within the thin film region far above the meniscus, and on the edges of the descending tears. This 'fine structure' was typically accompanied by weak surface deformation. It is important to note that the presence of Kalliroscope did not visibly alter the form of the surface deformation and so may be thought of as a passive tracer in our studies.

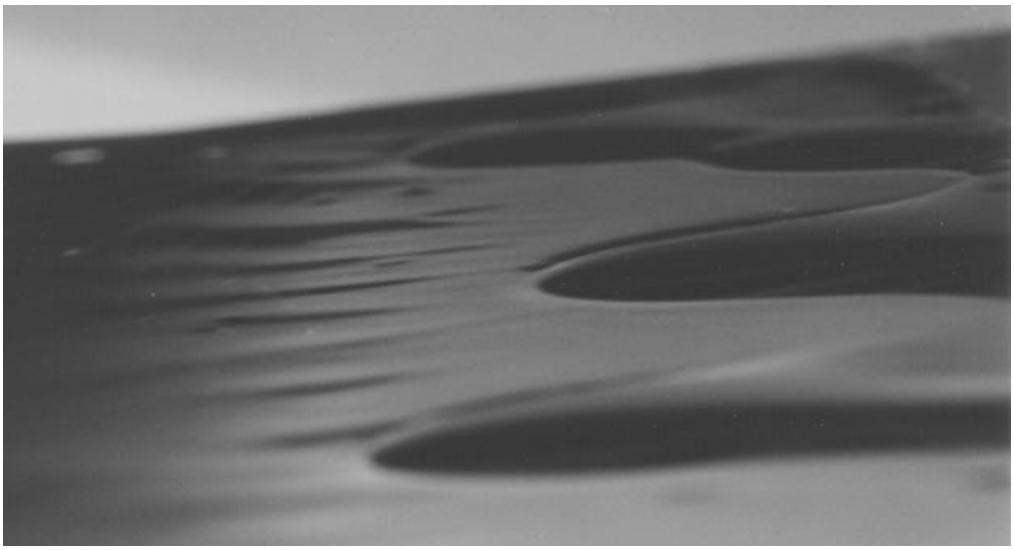

FIGURE 3. Photo of the tears and ridges: an oblique perspective of the meniscus region between the reservoir (left) and the adjoining thin film (right) on a plate inclined at 4° relative to the horizontal. Note the three descending tears, the surface deformations corresponding to the ridges, and the forking on the large central ridge which is beginning to exhibit dendritic structure. The horizontal scale is 8 cm and the fluid is 65% methanol and 35% water.

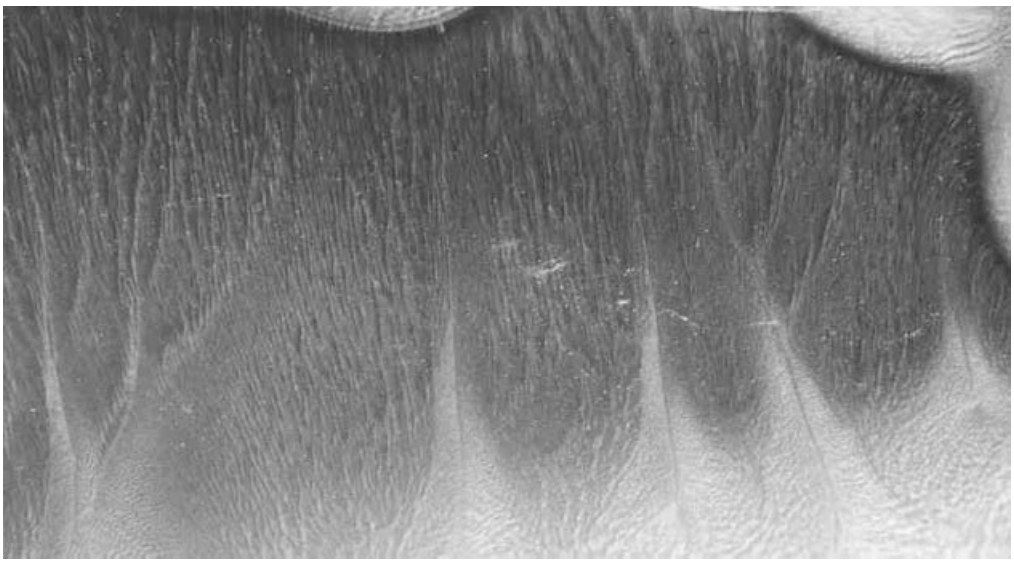

FIGURE 4. A plan view illustrating the reservoir (bottom), the thin film region (middle) and the incipient tear line (top). Kalliroscope reveals convection throughout. The ridges are the four white triangular structures at the lower right. Each ridge has a clearly visible dark spine which corresponds to a line of surface convergence and downwelling. The fine-scale convection is marked by light streaks further up the plate, and the irregular convection in the deep reservoir can be seen in the lower right corner. The horizontal scale is 6 cm and the fluid is 65% methanol and 35% water.

The ridges were found to align for any non-zero slope angle, and to exist even when the bounding wall was vertical, which is clear evidence that the convection is Marangoni rather than Rayleigh–Bénard: if the convective instability were buoyancy driven, it would disappear on a vertical plate. A series of experiments was also

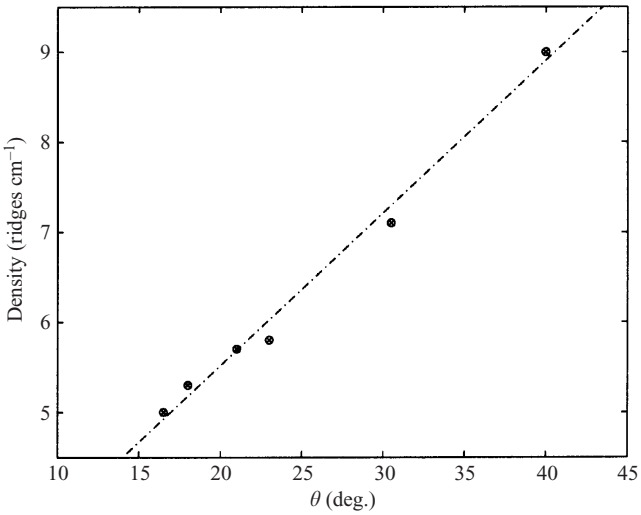

FIGURE 5. Density of ridges in the meniscus region versus inclination angle for 30% methanol, 70% water solutions.

conducted in order to test our hypothesis that the ridges result from the sheared Marangoni convection. A thin layer of methanol–water solution was placed on a horizontal interface, and randomly oriented Marangoni convection cells were evident. An applied radial wind stress was observed to align the convection rolls. The initially randomly oriented convection rolls could also be aligned by a radial thermocapillary stress generated by placing a cool metal cylinder in the centre of the film.

The dependence of the ridge spacing on inclination angle was examined, and the results are reported in figure 5. The trend of ridge density increasing with slope angle is commensurate with the observations of Vuilleumier *et al.* (1995). Conversely, the wavelength of the convection rolls associated with the fine structure was observed to weakly increase with θ. When the inclination angle of the plate was sufficiently small ($\theta < 3^\circ$), a striking dendritic free surface structure was apparent: the primary ducts were adjoined by secondary ducts aligned roughly perpendicular to the primary ducts (figure 6), and occasionally tertiary ducts aligned perpendicular to the secondary ducts.

For near vertical inclinations, we observed a second type of free-surface deformation corresponding to waves aligned perpendicular to the flow direction and propagating up the plate. Similar wave patterns were reported by Volkoviski (1935) who examined thermocapillary flow from a warm reservoir onto a cool tilted plate. In our experiments the waves only arose in the upper regions of the plate, at least 3 cm above the meniscus. The wavelength was observed to be less than 1 mm and the wave speed comparable to the rate of upflow.

Table 2 summarizes our experimental observations: specifically, when ridges, transverse waves, longitudinal rolls (fine structure) and tears were observed. Such structures were entirely absent in water. The structures observed in pure ethanol were markedly less pronounced than those in the binary system and were possibly evidence of evaporatively driven thermal rather than compositional Marangoni convection. Alternatively, these structures may be driven by compositional variations due to the absorption of atmospheric water.

		Flat plate	Tilted plate	Vertical plate
Ethanol	tears	–	✓	✓
	ridges	–	✓	✓
	fine	✓	D	N
Methanol $+H_2O$	tears	–	✓	✓
	ridges	–	✓	✓
	fine	✓	L,T,D	T,L
Ethanol $+H_2O$	tears	–	✓	✓
	ridges	–	✓	✓
	fine	✓	L,T,D	T,L
H_2O	tears	–	–	–
	ridges	–	–	–
	fine	–	–	–

TABLE 2. A summary of our experimental results. 'Fine' refers to the fine-scale structure in the thin film above the ridges characterized by either transverse waves or longitudinal rolls. ✓: effect was observed; –: effect was not observed; N: no thin film (insufficient surface stress); T: transverse waves; D: dendritic structure; L: stationary rolls, aligned with shear.

FIGURE 6. Plan view of the dendritic free-surface structure evident in a 50% methanol, 50% water solution climbing a 3° slope. The flow is from bottom to top, and the horizontal extent of the image is 5 cm. The free surface deformations are rendered visible with a shadowgraph.

Evaporation rates were measured by placing a shallow vessel filled with alcohol or an alcohol–water solution on a balance. The mass was recorded at intervals of one minute and the results are summarized in figure 7. This plot illustrates that the evaporation rate was approximately constant throughout each of our experiments.

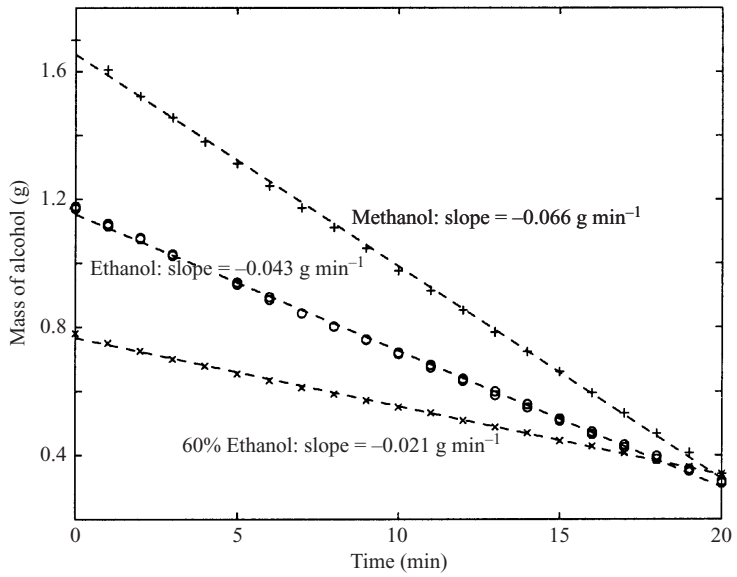

FIGURE 7. Evaporation rate of various pure alcohols and alcohol–water solutions. The surface area exposed to the atmosphere is $\sim 10\,\mathrm{cm}^2$. All measurements were taken at atmospheric pressure and room temperature. The evaporation rate remained constant as the thickness varied from millimetres to microns, well within the range of thicknesses observed in our tilted plate experiments.

3. Physical picture

Apart from the apparent deflection of the free surface, the observed planform of convection takes precisely the form described by Smith & Davis (1983*a*) in a horizontal Marangoni shear layer at large Prandtl numbers. We thus assess the viability of their mechanism of convection in our system. In the limit of zero surface conductivity, Smith & Davis (1983*a*) compute a critical 'shear Marangoni number', $\mathscr{M}_s = \tau H^2/\mu\kappa$ for two types of velocity profiles: one that is linear in z and a 'return flow' that is quadratic. In the case of linear flow, they find the critical shear Marangoni number asymptotes to 15 at large Prandtl number. However, for return flow, they find that the system is stable to longitudinal rolls for all values of $\mathscr{M}_s$. Evaluating an analogous compositional Marangoni number from our system parameters (see table 3) yields

$$\mathscr{M}_s = \frac{\tau H^2}{\mu D} \sim \frac{0.5 \times (2 \times 10^{-3})^2}{10^{-2} \times 10^{-5}} \sim 10. \tag{3.1}$$

Note that in our system, the surface stress is associated with compositional rather than thermal gradients (Vuilleumier *et al.* 1995). Since τ and H are measured experimentally and the ratio of molecular diffusivity, D, to thermal diffusivity, κ, is $D/\kappa = (1.26 \times 10^{-5}\,\mathrm{cm}^2\,\mathrm{s}^{-1})/(1.5 \times 10^{-3}\,\mathrm{cm}^2\,\mathrm{s}^{-1}) \sim 10^{-2}$, the thermal Marangoni number is two orders of magnitude smaller than $\mathscr{M}_s$. Our flow profile can be written as a linear combination of the two velocity profiles considered by Smith & Davis (1983*a*) so we expect the critical Marangoni number in our system to be finite but greater than 15. Although the convective instability mechanism of Smith & Davis (1983*a*) is potentially significant in our experiments, it is important to note that their theoretical model neglects gravity as well as the most salient feature of our flows, namely, surface deflection. Consequently, we develop a model of convective instability in our

	Symbol	Value
Film thickness	H	20–100 μm$^{\dagger *}$
Horizontal length scale	L	$\sim$ 1 cm*
Speed up the plate	U	$\sim$ 1 mm s$^{-1\dagger *}$
Diffusivity of alcohol in water	D	1.26×10^{-5} cm^2 s$^{-1\ddagger}$
Thermal diffusivity	κ	1.5×10^{-3} cm^2 s$^{-1\ddagger}$
Coefficient of thermal expansion	β	2.2×10^{-4} °C$^{-1\ddagger}$
Viscosity of alcohol/water mixtures	μ	0.006–0.01 g cm^{-1} s$^{-1\ddagger}$
Evaporation rate	E	3.5×10^{-5} g s^{-1} cm^{-2*}
Surface tension of alcohol/water mixtures	σ	25–70 dyn cm$^{-1\ddagger}$
Density of alcohol/water mixtures	ρ	0.8–1 g cm^{-3}
Change in surface tension due to concentration	α	$\sim$ 25 dyn cm$^{-1\ddagger}$
Change in density due to concentration	$\partial\rho/\partial c$	$\sim$ 0.2 g cm$^{-3\ddagger}$
Change in surface tension due to temperature	$\partial\sigma/\partial T$	$\sim$ 0.2 dyn cm^{-1} °C$^{-1\ddagger}$

TABLE 3. Estimated values for parameters in experiments. † from Vuilleumier *et al.* (1995), * from experiments by the authors, ‡ CRC values (Lide 1974). Concentration is measured by volume fraction.

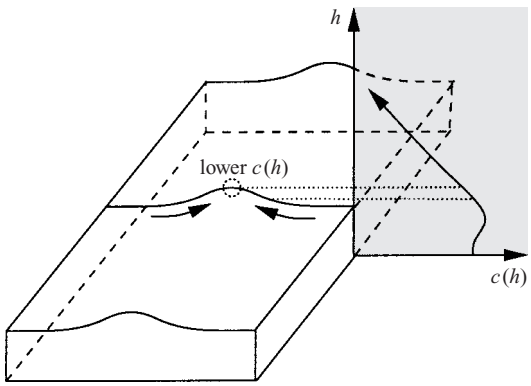

FIGURE 8. The mechanism driving the longitudinal rolls. The base concentration profile is set by evaporation from the free surface, diffusion across the layer and convection up the plane. In certain parameter regimes, thicker regions have lower concentrations at the free surface; thus surface tension may be higher in the elevated regions and so render the system unstable to Marangoni convection.

system which relies explicitly on the interplay between surface deformations and the destabilizing concentration profile. Our analysis demonstrates that, as in Scriven & Sternling's (1964) extensions of Pearson's (1958) model, the inclusion of free-surface deformations serves to destabilize the system of Smith & Davis (1983*a*); however, as made clear in Smith's (1966) contribution to the Pearson (1958) model, this destabilizing influence may be mitigated by the inclusion of gravity.

We proceed by examining a model that relies explicitly on the interplay between the deformable free surface and the steady-state concentration profile which is set by balancing diffusion, evaporation, and convection up the plate. The concentration is depleted near the surface by evaporation; nevertheless the system remains in a quasi-steady state because the evaporating alcohol is replenished by fresh fluid convected up from the reservoir. Qualitatively this leads to a vertical concentration profile similar to that sketched in figure 8. If the surface is locally perturbed upwards and

the concentration profile adjusts to its basic-state profile faster than the interface relaxes, the concentration on the bump is lower than in the neighbouring regions. The resulting surface tension gradient draws fluid into the bump and the film is destabilized. Similarly, depressions in the free surface lead to local minima in surface tension which pull fluid away from depressed areas. The resulting flow enhances the surface deformations and sustains convection (see figure 8). This argument will be made quantitative in § 4.

This physical picture relies on relatively fast diffusive timescales across the film. If the interface is perturbed upwards, the concentration profile must adjust to the new height before the elevated region can relax back to a flat profile. Thus if $t_{\text{diff}}/t_{\text{relax}} \ll 1$ the system is unstable; t_{relax} can be estimated by balancing pressure and viscous stresses, $\nabla p \sim (\mu/H^2)U \sim (\mu/H^2)L/t_{\text{relax}}$. The restoring pressure gradient is dictated by surface tension or gravity, $p \sim \sigma H/L^2$ or $p \sim \rho g H$, respectively. Taking the ratio of the appropriate timescales yields:

$$\text{surface tension restoring pressure} \quad \frac{t_{\text{diff}}}{t^{\sigma}_{\text{relax}}} = \left(\frac{H}{L}\right)^4 \frac{\sigma H}{D\mu} \sim 10^{-4},$$

$$\text{gravitational restoring pressure} \quad \frac{t_{\text{diff}}}{t^{g}_{\text{relax}}} = \left(\frac{H}{L}\right)^2 \frac{H^3 \rho g}{D\mu} \sim 10^{-2}.$$

Since both of these dimensionless groups are substantially less than one, we infer that our system is potentially unstable to Marangoni convection driven by surface deformations.

4. Mathematical model

The geometry with relevant coordinates is illustrated in figure 1. We will develop a simplified mathematical model to describe the dynamics in the thin film. Based on data from Vuilleumier *et al.* (1995) and our own experiments, it is reasonable to assume that gradients along $\hat{\boldsymbol{y}}$ are much smaller than those along $\hat{\boldsymbol{x}}$ and $\hat{\boldsymbol{z}}$; consequently we will consider a quasi-two-dimensional film with negligibly small variations in the $\hat{\boldsymbol{y}}$-direction.

4.1. *Concentration profile*

To establish a base profile, we consider a film being drawn up the plate with no velocity component or variations in the $\hat{\boldsymbol{x}}$-direction and negligibly slow variations along $\hat{\boldsymbol{y}}$. Note that although we are restricting ourselves to small gradients in $\hat{\boldsymbol{y}}$, we are not imposing any restrictions on the velocity in the $\hat{\boldsymbol{y}}$-direction which is comparable to the largest velocities in the problem. Let $\boldsymbol{u} = (u, v, w)$ and assume that $u = w = 0$ and $v = v(z)$. We solve the steady-state problem of a film being drawn up a plate where the density, ρ, is constant (not a function of alcohol concentration, c) and the surface tension, σ, is a linear function of concentration:

$$\sigma(c) = \sigma_0 - \alpha(c - c_0) \tag{4.1}$$

where $\alpha = -(\partial\sigma/\partial c)|_{c=c_0}$ and c_0 is the concentration in the reservoir; α is positive since surface tension decreases with alcohol concentration. Motivated by the experimental evidence of Vuilleumier *et al.* (1995), we consider a constant surface stress, τ, due to the slowly varying concentration in the y-direction, which drives flow up the plate. The following analysis will demonstrate that a constant surface stress is consistent with both the fluid and concentration equations. The steady-state flow profile up

the plate is then deduced by balancing viscosity and gravity with a constant stress boundary condition at the free surface $z = h$:

$$\mu v_{zz} = \rho g \sin\theta \quad \text{and} \quad \mu v_z|_{z=h} = \tau. \tag{4.2}$$

We note that the influence of capillary pressure has been neglected, an approximation which is valid sufficiently far from the meniscus (Vuilleumier *et al.* 1995). The velocity profile up the plate is given by

$$\mu v = \rho g \sin\theta \left(\tfrac{1}{2}z^2 - hz\right) + \tau z. \tag{4.3}$$

In the absence of gravity this reduces to the linear shear profile examined by Smith & Davis (1983*a*). However if $\theta \neq 0$ gravity resists the upflow causing the velocity profile to sag. This sagging effect prescribes the maximum film thickness, $H_{\max}$, that can be sustained by the surface stress, τ; the film can exist in steady state only if the flux up the plate, q, is positive:

$$q = \int_0^h v(z)\mathrm{d}z = \frac{\tau}{2\mu}h^2 - \frac{\rho g}{3\mu}\sin\theta h^3 > 0 \quad \Rightarrow \quad H_{\max} = \frac{3}{2\sin\theta}\frac{\tau}{\rho g}. \tag{4.4}$$

Using values from table 3 suggests a maximum film thickness on a vertical plate to be on the order of 100 μm which is in accord with experimental evidence.

The concentration profile is derived from a steady-state convection–diffusion equation, $\boldsymbol{u}\cdot\nabla c = D\nabla^2 c$ where D is the diffusivity of alcohol in water. Since we have imposed $u = w = 0$ and $\tau \sim c_y = \text{constant}$, we consider

$$v c_y = D c_{zz}. \tag{4.5}$$

We apply boundary conditions appropriate for a no-flux boundary condition at $z = 0$

$$\left.\frac{\partial c}{\partial z}\right|_{z=0} = 0 \tag{4.6}$$

and a constant flux due to evaporation at the free surface

$$-\left.\frac{\partial c}{\partial z}\right|_{z=h} = Q \tag{4.7}$$

where Q is a parameter that depends on the temperature and on the microscopic properties of the mixture such as heat of vaporization and chemical conductivity (Carey 1992). Following our experimental data, we choose Q to be constant (see figure 7), thus neglecting the higher-order influences of vapour pressure, curvature and concentration on the evaporation rate. Integrating (4.5) with respect to z and applying the boundary condition at $z = 0$ yields

$$c = -\frac{\tau}{\alpha}y - \frac{\tau}{\alpha D\mu}\left[\rho g \sin\theta(\tfrac{1}{24}z^4 - \tfrac{1}{6}hz^3) + \tfrac{1}{6}\tau z^3\right] + c_0. \tag{4.8}$$

Note that in the limit of $D \to \infty$, there is no gradient in c across the layer and the film is stable to Marangoni convection. Applying the upper boundary condition (4.7) uniquely prescribes the surface stress τ. In particular, τ is given by

$$\tau = \rho g H\frac{\sin\theta}{3} + \sqrt{\left(\rho g H\frac{\sin\theta}{3}\right)^2 + 2\frac{D\mu}{H^2}\alpha Q}. \tag{4.9}$$

Note that there are no free parameters in the system: the surface stress is uniquely determined by the evaporation rate, gravity, average film thickness and fluid properties.

4.2. *Long-wavelength approximation*

Having found a base-state profile, we proceed by considering long-wavelength variations in the $\hat{\boldsymbol{x}}$-direction. Since the surface deformations observed in our experiments are typically millimetric while the layer depth is $< 100\,\mu$m, it is reasonable to develop a lubrication or long-wavelength model. Initially we consider a three-dimensional system, again assuming slow variations, but non-zero velocity, in the $\hat{\boldsymbol{y}}$-direction. Since the reduced Reynolds number, $\mathscr{R}e(H/L) = \rho H^2 U/(L\mu) = \rho\tau H^3/(L\mu^2) \sim O(10^{-4})$, is small we consider an incompressible Stokes flow:

$$\nabla p = \mu\nabla^2 \boldsymbol{u} + \rho \boldsymbol{g}, \tag{4.10}$$

$$\nabla \cdot \boldsymbol{u} = 0. \tag{4.11}$$

The boundary conditions at the free surface are given by normal and tangential stress balances:

$$\hat{\boldsymbol{n}} \cdot \boldsymbol{T} \cdot \hat{\boldsymbol{s}} = \nabla_s \sigma,$$

$$\hat{\boldsymbol{n}} \cdot \boldsymbol{T} \cdot \hat{\boldsymbol{n}} = \sigma \nabla \cdot \hat{\boldsymbol{n}},$$

where $\hat{\boldsymbol{n}}$ is the unit normal to the free surface, $\hat{\boldsymbol{s}}$ is the unit tangent to the free surface, $\nabla_s = (\boldsymbol{I} - \hat{\boldsymbol{n}}\hat{\boldsymbol{n}}) \cdot \nabla$ is the surface gradient operator and $\boldsymbol{I}$ is the identity matrix. $\boldsymbol{T}$, the stress tensor with y-derivatives neglected, is given by

$$\boldsymbol{T} = \begin{pmatrix} -p + 2\mu u_x & \mu v_x & \mu(u_z + w_x) \\ \mu v_x & -p & \mu w_z \\ \mu(u_z + w_x) & \mu w_z & -p + 2\mu w_z \end{pmatrix}. \tag{4.12}$$

We apply no-slip boundary conditions at the plate.

To simplify this system, we rescale the equations above and apply a long-wavelength approximation. The resulting equations will be solved order by order for velocity and pressure which will be averaged across the depth of the film. The resulting equation will be a spatially one-dimensional fourth-order partial differential equation for the height of the free surface. We will find that gravity and capillarity appear in their standard lubrication form along with a more unusual destabilizing term due to evaporatively driven Marangoni forcing.

The variables are rescaled as follows:

$$\left.\begin{aligned} (u, v) &= U(\tilde{u}, \tilde{v}), \quad & w &= \epsilon U \tilde{w}, \\ (x, y) &= L(\tilde{x}, \tilde{y}), \quad & z &= H\tilde{z}, \\ p &= (U\mu/H)\tilde{p}, \quad & t &= [H/(U\epsilon^2)]\tilde{t}. \end{aligned}\right\} \tag{4.13}$$

The resulting non-dimensional groups are listed in table 4. U is a typical velocity driven by the stress at the free surface in the $\hat{\boldsymbol{y}}$-direction, $U = \tau H/\mu$. Note that the Prandtl number, $\mathscr{P}r = \nu/D$, is not an independent parameter in our system and can be defined by $\mathscr{M}_s = \mathscr{R}e\,\mathscr{P}r$. We are investigating flows at fixed Marangoni number in the limit $\mathscr{R}e \to 0$, thus our analysis is restricted to large-Prandtl-number fluids, $\mathscr{P}r \to \infty$, such as those examined experimentally

Rescaling the fluid equations above using (4.13) and dropping the tildes, we reduce Stokes equation to

$$\epsilon p_x = \epsilon^2 u_{xx} + u_{zz}, \tag{4.14}$$

$$0 = \epsilon^2 v_{xx} + v_{zz} - \mathscr{S} \sin\theta, \tag{4.15}$$

$$p_z = \epsilon^3 w_{xx} + \epsilon w_{zz} - \mathscr{S} \cos\theta. \tag{4.16}$$

Dimensionless group	Symbol	Definition	Order of magnitude
Marangoni number	$\mathscr{M}_s$	$\frac{\tau H^2}{D\mu}$	10
	$\mathscr{S}$	$\frac{H\rho g}{\tau}$	1
Capillary number	$\mathscr{C}$	$\epsilon^2\frac{\sigma}{\mu U}$	10^{-3}
Prandtl number	$\mathscr{P}r$	$\frac{\nu}{D}$	10^3
Reynolds number	$\mathscr{R}e$	$\frac{\rho\tau H^2}{\mu^2}$	10^{-2}
Bond number	$\mathscr{B}$	$\frac{\rho g L^2}{\sigma}$	10
Aspect ratio	ϵ	$\frac{H}{L}$	10^{-3}

TABLE 4. Relevant dimensionless groups evaluated using the parameter values given in table 3.

Here p has been rescaled such that the dominant balance in the $\hat{\boldsymbol{z}}$-direction is between pressure and gravity; thus, hydrostatic pressure will appear at lowest order. The divergence-free condition becomes

$$u_x + w_z = 0. \tag{4.17}$$

Tangential stress balances in the $\hat{\boldsymbol{x}}$- and $\hat{\boldsymbol{y}}$-directions (at $z = h$) are

$$(1-\epsilon^2 h_x^2)(u_z + \epsilon^2 w_x) + 2\epsilon^2 h_x(w_z - u_x) = -c_x\sqrt{1+\epsilon^2 h_x^2}, \tag{4.18}$$

$$v_z - \epsilon^2 h_x v_x = -c_y\sqrt{1+\epsilon^2 h_x^2}, \tag{4.19}$$

respectively. Normal stress balance (at $z = h$) gives

$$-p + \frac{2}{(1+\epsilon^2 h_x^2)}[\epsilon^3 h_x^2 u_x + \epsilon w_z - \epsilon h_x(u_z + \epsilon^2 w_x)] = (\mathscr{C} - \epsilon c)\frac{h_{xx}}{(1+\epsilon^2 h_x^2)^{3/2}}, \tag{4.20}$$

the no-slip boundary condition at $z = 0$ becomes

$$u = v = w = 0, \tag{4.21}$$

and the concentration equation (4.8) becomes

$$c = -y - \epsilon\mathscr{M}_s\left[\mathscr{S}\sin\theta\left(\tfrac{1}{24}z^4 - \tfrac{1}{6}hz^3\right) + \tfrac{1}{6}z^3\right] + c_0. \tag{4.22}$$

Dimensionless concentration profiles are plotted in figure 9. Note that if the free surface is perturbed upwards away from the steady state $H = 1$, the concentration decreases if $\mathscr{S}\sin\theta < 1$. By the physical argument in § 3, we expect this scenario to be unstable since low concentration leads to high surface tension in the thicker parts of the film. Thus the film is always stable if $\mathscr{S}\sin\theta > 1$.

Expanding $\boldsymbol{u}$ and p in powers of ϵ,

$$\boldsymbol{u} = \boldsymbol{u}_0 + \epsilon\boldsymbol{u}_1 + \epsilon^2\boldsymbol{u}_2\cdots, \tag{4.23}$$

$$p = p_0 + \epsilon p_1 + \epsilon^2 p_2\cdots, \tag{4.24}$$

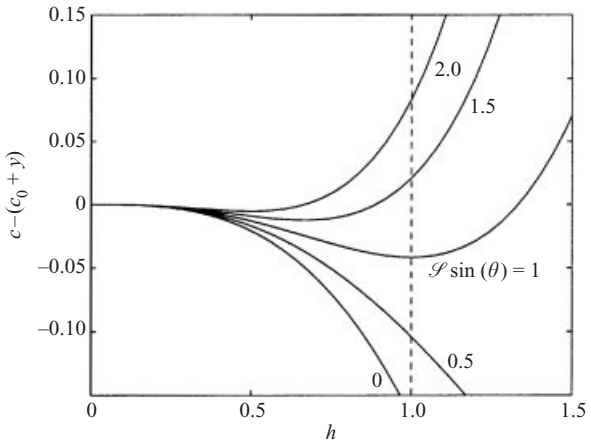

FIGURE 9. The variations in surface concentration versus dimensionless film thickness for $\epsilon\mathscr{M}_s = 1$ and various values of $\mathscr{S}\sin\theta$. Note that if the film thickness is increased beyond its average value ($H = 1$), the concentration decreases only if $\mathscr{S}\sin\theta < 1$; consequently, convection may be sustained only if the surface tension gradient is sufficiently large.

equations (4.14)–(4.22) can be solved analytically order by order for the velocities and the pressures in terms of $h(x)$ (see the Appendix). To $O(1)$, $\boldsymbol{u}_0$ and p_0 are given by

$$\left.\begin{aligned} &u_0 = 0, \quad v_0 = \mathscr{S}\sin\theta\left(\tfrac{1}{2}z^2 - hz\right) + z, \quad w_0 = 0, \\ &p_0 = \mathscr{S}\cos\theta(h - z) - \mathscr{C}h_{xx}. \end{aligned}\right\} \tag{4.25}$$

This lowest-order flow corresponds to the base state derived in § 4.1. The flow is quadratic and purely parallel to the plate in the $\hat{\boldsymbol{y}}$-direction, pulled upwards by surface stresses and resisted by gravity. The flow is purely up the plate with no inflection point if $\mathscr{S}\sin\theta < 1$. At next order, $O(\epsilon)$, the velocities and pressures are given by

$$\left.\begin{aligned} u_1 &= (\mathscr{S}\cos\theta h_x - \mathscr{C}h_{xxx})\left(\tfrac{1}{2}z^2 - hz\right) + \tfrac{1}{2}h^2\mathscr{M}_s(1 - \mathscr{S}h\sin\theta)h_x z, \\ v_1 &= 0, \\ w_1 &= -\left[(\mathscr{S}\cos\theta h_x - \mathscr{C}h_{xxx})\left(\tfrac{1}{6}z^3 - \tfrac{1}{2}hz^2\right) + \tfrac{1}{4}h^2\mathscr{M}_s(1 - \mathscr{S}h\sin\theta)h_x z^2\right]_x, \\ p_1 &= (c_0 - y)h_{xx}. \end{aligned}\right\} \tag{4.26}$$

The final step is to calculate the height of the free surface. To find $h(x)$, we average over the depth and use conservation of mass. The continuity equation for our quasi-two-dimensional system may be expressed as

$$\epsilon h_t + \left(\int_0^{h(x)} u_0 + \epsilon u_1 + \epsilon^2 u_2 \,\mathrm{d}z\right)_x + \epsilon^2\mathscr{E} + \mathscr{O}(\epsilon^3) = 0 \tag{4.27}$$

where $\mathscr{E} = EL^2/(\epsilon UH^2\rho)$ is the dimensionless mass loss due to evaporation. Using the velocities from (4.25) and (4.26) and keeping terms to $\mathscr{O}(\epsilon)$, we obtain a partial differential equation for $h(x)$,

$$h_t + \left[\tfrac{1}{3}h^3(\mathscr{C}h_{xxx} - \mathscr{S}\cos\theta h_x) + \tfrac{1}{4}\mathscr{M}_s h^4 h_x(1 - \mathscr{S}h\sin\theta)\right]_x = 0. \tag{4.28}$$

This equation will be solved numerically in § 5. The first two terms in the brackets represent capillarity and gravity, respectively, both of which are stabilizing. The third term represents the potentially destabilizing Marangoni surface stress and the fourth

is a stabilizing term that appears in the Marangoni forcing owing to the influence of gravity on the velocity field. Increasing gravity decreases the alcohol transport from the reservoir and diminishes concentration gradients across the film, thus potentially stabilizing the film to Marangoni convection.

4.3. *Linear stability analysis: longitudinal rolls*

Before investigating (4.28) numerically, it will prove instructive to analyse its linear stability properties. To determine the most unstable wavelength, we perform a linear stability analysis about the base state $h(x) = 1$ through examining small perturbations of the form

$$h(x) = 1 + \delta\bar{h}(x,t). \tag{4.29}$$

Substituting h into (4.28) yields

$$\bar{h}_t + \left[\tfrac{1}{4}\mathscr{M}_s(1 - \mathscr{S}\sin\theta) - \tfrac{1}{3}\mathscr{S}\cos\theta\right]\bar{h}_{xx} + \tfrac{1}{3}\mathscr{C}\bar{h}_{xxxx} = 0. \tag{4.30}$$

We seek solutions of the form $\bar{h}(x,t) = \mathrm{e}^{\gamma t}\cos(kx)$ and find an expression for the growth rate, γ:

$$\gamma = \tfrac{1}{4}\mathscr{M}_s(1 - \mathscr{S}\sin\theta)k^2 - \tfrac{1}{3}\mathscr{C}k^4 - \tfrac{1}{3}\mathscr{S}k^2\cos\theta. \tag{4.31}$$

Perturbations will decay if $\gamma < 0$; consequently, the film is stable to perturbations at any wavelength provided

$$\tfrac{1}{3}\mathscr{S}\cos\theta > \tfrac{1}{4}\mathscr{M}_s(1 - \mathscr{S}\sin\theta). \tag{4.32}$$

If this condition is not met, then there will be some wavenumbers that will grow exponentially. Notice that the capillary number, $\mathscr{C}$, does not enter into this criterion. Ultimately gravity determines the cutoff for stability and surface tension only enters in selecting the most unstable wavelength. The most unstable wavenumber maximizes γ and can be deduced from the quadratic that results from setting $\mathrm{d}\gamma/\mathrm{d}k = 0$:

$$k_{\mathrm{crit}} = \sqrt{\left[\tfrac{3}{8}\mathscr{M}_s(1 - \mathscr{S}\sin\theta) - \tfrac{1}{2}\mathscr{S}\cos\theta\right]/\mathscr{C}}. \tag{4.33}$$

Sample plots of wavelength versus average film thickness are given in figure 10, where parameters correspond to the range relevant in our experiments. The predicted wavelengths are consistent with those of the rolls observed in the thin film region. Figure 10 indicates that the minimum ratio of roll width to layer depth is approximately 5 : 1; thus the convection cells have a skewed aspect ratio (rolls are long and flat) which is consistent with our long-wavelength approximation. It is important to note that this result for the most unstable mode predicts increasing wavelength with inclination angle, a prediction which agrees qualitatively with observations of the fine structure. This result is not expected to explain the dependence of ridge spacing on θ (illustrated in figure 5), as the ridges are fully developed nonlinear surface features. As observed in our experiments and measured explicitly by Fanton & Cazabat (1998), the ridges undergo a coarsening period in which the initial wavelength evolves and eventually saturates as the ridges merge. One would not expect the predictions of a linear analysis to be commensurate with the saturated lengthscales observed experimentally. The disparity in lengthscales between the most unstable wavelength and the ridge spacing is evident in our numerical study presented in § 5.

Two cases of particular interest are that of a flat plate ($\theta = 0$) and a vertical plate ($\theta = \pi/2$). For a flat plate the stability criterion (4.32) becomes $\mathscr{S} > \frac{3}{4}\mathscr{M}_s$ or in

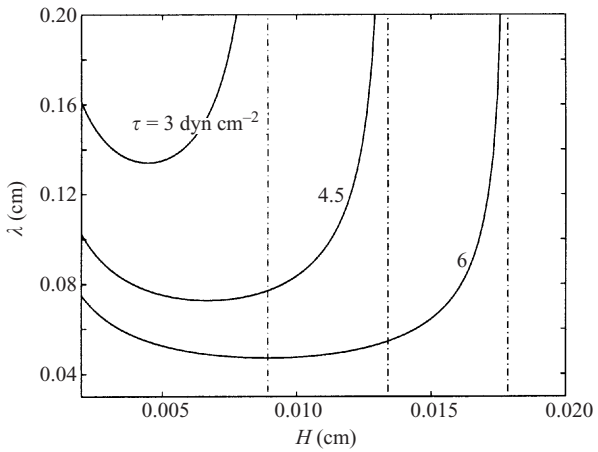

FIGURE 10. Most unstable wavelength, λ, as a function of average layer depth, H, for various realistic values of τ. The dashed-dotted lines represent $\mathscr{S}\sin\theta = 1$ for each value of τ; we require that $\mathscr{S}\sin\theta < 1$ for the film to be unstable to longitudinal rolls. Here $\theta = 0.35$ rad, $D = 1.26 \times 10^{-5}\,\mathrm{cm^2\,s^{-1}}$, $\mu = 0.01\,\mathrm{g\,cm^{-1}\,s^{-1}}$, $\sigma = 27\,\mathrm{dyn\,cm^{-1}}$ and $\alpha = 25\,\mathrm{dyn\,cm^{-1}}$.

dimensional form

$$\frac{4}{3} > \frac{\tau^2 H}{D\mu\rho g} \quad \text{(flat plate stability)}. \tag{4.34}$$

The film is stabilized by gravity, which acts to resist the surface deformation critical in driving the instability, and diffusion, which acts to flatten out the concentration profile. As the film becomes thin, diffusion across the layer dominates convective transport up the plate in determining the concentration profile. Consequently, the layer is stable in the limit of $H \to 0$, a result which is markedly different from the quiescent layer result of Smith (1966). For a vertical plate, the stability criterion becomes $\mathscr{S} > 1$ and $\mathscr{M}_s > 0$ or

$$\frac{\rho g H}{\tau} > 1 \quad \text{and} \quad \frac{\tau H^2}{D\mu} > 0 \quad \text{(vertical plate stability)}. \tag{4.35}$$

Again the surface is destabilized by surface stresses and stabilized by gravity. Note that the vertical plate stability criterion corresponds to the criterion for an inflection point in the flow. Thus flow profiles on a vertical plate with no inflection point are always unstable to compositional Marangoni convection.

4.4. *Transverse waves*

Finally, to include transverse waves in our stability framework, we adopt the results of Smith & Davis (1983*b*) who analysed transverse surface deformations in thermally driven horizontal shear flows and deduced the following criterion for stability:

$$\left(\frac{2}{15}v_{zz} + \frac{1}{2}\frac{\mu c_p}{k_s H}v_z\right)(v_{zz} - v_z)\bigg|_{z=h=1} \leqslant 0, \tag{4.36}$$

where c_p is the specific heat and k_s the thermal surface conductance. Since their results apply to flow in zero gravity, we expect this criterion to be relevant when the plate is near vertical; in this case, near the onset of instability, gravitational effects will be important in determining the basic flow profile but less influential in damping out normal deformations of the interface. Substituting our velocity profile (4.25) into

(4.36) yields the stability criterion:

$$(\mathscr{S}\sin\theta - 1) \leqslant 0. \tag{4.37}$$

From § 4.1 we know that the film can only be sustained when $\mathscr{S}\sin\theta < 3/2$. Thus we expect transverse waves when

$$1 < \mathscr{S}\sin\theta < \tfrac{3}{2} \quad \text{(unstable to transverse waves)}. \tag{4.38}$$

Note that these waves only occur when there is an inflection point in the flow, i.e. when surface stresses and gravity are comparable. Vuilleumier *et al.*'s (1995) experimental data show a gradual decrease in concentration gradients, hence surface stresses, as one moves up the plate; this suggests, in conjunction with (4.38), that transverse waves will be most likely to appear far from the meniscus. The stability criterion also implies that these waves should be most prevalent at large θ. Both of these trends are consistent with our experimental observations. The complete stability picture is summarized in figure 14 and will be discussed in § 6.

5. Numerical results

Equation (4.28) was solved numerically using centred finite differences with an implicit timestep and periodic boundary conditions in x. We used a uniform mesh in space and controlled the timestep via step-doubling. The fourth-order equation was rewritten as two second-order equations by defining $f = h_{xx}$; f and h are both knot-centred quantities. Fluxes were evaluated at the centre of each interval using averaged quantities and nonlinear terms were evaluated by averaging first, for example,

$$h_{i+1/2}^2 = \left(\frac{h_i + h_{i+1}}{2}\right)^2. \tag{5.1}$$

5.1. *Ridge formation*

Computations show that, starting with a small, random perturbation superimposed on a flat initial state, ridges form rapidly and evolve into a 'quasi-steady' state. Figure 11 shows two time series that illustrate the formation and subsequent nonlinear evolution of the ridges; we show a series of snapshots of the free surface at regular time intervals where each successive profile has been shifted upwards. Initially the wavelength is in accord with the linear predictions given by (4.33) (for these parameters, linear stability predicts eight ridges). However, as the ridges grow, nonlinear effects become important and the ridge structures may wander sideways and merge. The merging events occur over a much longer timescale than that of formation so we refer to the intermediary states as 'quasi-steady'. The timescale in plot (*b*) is two orders of magnitude larger than that in (*a*). This long timescale allows us to observe the meandering motions of the mature ridges.

5.2. *Ridge structure*

The streamlines within one ridge are shown in figure 12. Each ridge is composed of two counter-rotating vortices with fluid being drawn up the sides and descending along the ridge centreline. Fluid in the film between the ridges is nearly stationary. Figure 13 shows the evolution of vorticity during the formation of two ridges. Initially, there is a very small vorticity component due to shear flow in the $\hat{\boldsymbol{y}}$-direction. Surface deformations are directly correlated with large vorticity.

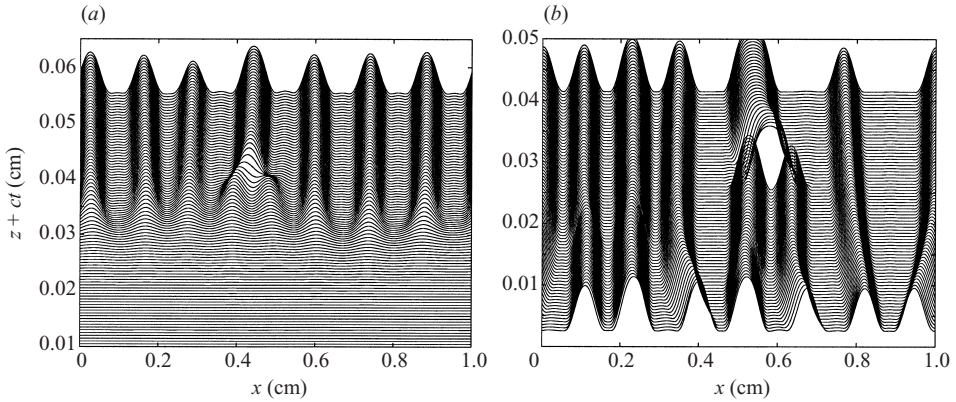

FIGURE 11. A numerical time series illustrating the formation and evolution of the ridges. Time is increasing in the vertical direction. In (*a*) and (*b*) the evolution of the film shape is traced for approximately 1 s and 1 min, respectively. (*a*) The initial profile at the bottom is a snapshot of the free surface at $t = 1.4 \times 10^{-6}$ (in rescaled dimensionless time). Profiles are then printed at intervals of $\Delta t = 1.0 \times 10^{-7}$ (= 0.002 s) and are shifted up by $c\Delta t = 5 \times 10^{-4}$ cm for each time. (*b*) The subsequent evolution of the ridges. Profiles are printed at intervals of $\Delta t = 2 \times 10^{-5}$ in dimensionless time (= 0.375 s). This longer timescale allows us to track the wandering motion of the ridges but it is not sufficiently fine to resolve the details of the rapidly merging ridges in the centre of the figure. Parameters used in these simulations are: $\mu = 0.01\,\mathrm{g\,cm^{-1}\,s^{-1}}$, $\tau = 3.3\,\mathrm{dyn\,cm^{-2}}$, $\sigma = 27\,\mathrm{dyn\,cm^{-1}}$, $\alpha = 25\,\mathrm{dyn\,cm^{-1}}$, $\theta = 0.45$ and $H = 0.003\,\mathrm{cm}$; this corresponds to dimensionless group values of $\epsilon = 0.0004$, $\mathscr{S} = 0.882$, $\mathscr{C} = 4.32 \times 10^{-4}$ and $\mathscr{M}_s = 238.1$ which are comparable to those in our experiments.

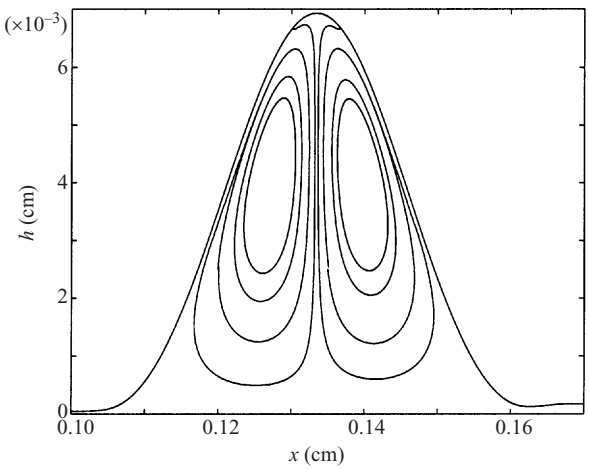

FIGURE 12. Streamlines showing counter-rotating vortices within one ridge. Flow ascends the sides of the ridge and descends through the centre. Parameters used in this simulation are: $\mu = 0.01\,\mathrm{g\,cm^{-1}\,s^{-1}}$, $\tau = 5\,\mathrm{dyn\,cm^{-2}}$, $\sigma = 27\,\mathrm{dyn\,cm^{-1}}$, $\Delta\sigma = 25\,\mathrm{dyn\,cm^{-1}}$, $\alpha = 0.45$ and $H = 0.002\,\mathrm{cm}$; this corresponds to dimensionless group values of $\epsilon = 0.0004$, $\mathscr{S} = 0.392$, $\mathscr{C} = 4.32 \times 10^{-4}$ and $\mathscr{M}_s = 159$.

6. Discussion

We have presented theoretical and experimental evidence for a class of convection which relies explicitly on the combined influence of background shear and surface deformation. The tendency of shear to align convection rolls in the direction of the mean flow has been established both theoretically and experimentally (Bénard 1927; Richter & Parsons 1975; Gumerman & Homsy 1974). In our system the shear

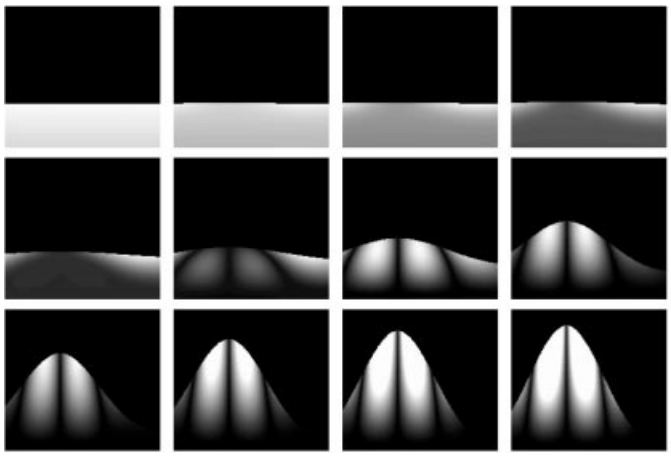

FIGURE 13. A time series showing the generation of total vorticity, $|\omega| = \sqrt{v_z^2 + v_x^2 + (w_x - u_z)^2}$ where white represents high vorticity and black low. Each panel uses a separate colour table with dimensionless vorticities ranging from $O(1)$ in the first few panels to $O(10^4)$ in the last. The series starts in the upper left corner and time increases moving to the right and down. The first image shows the initial vorticity at $t = 0$ which is almost zero. Subsequently, vorticity is plotted at intervals of $t = 4 \times 10^{-7}$ starting with $t = 6 \times 10^{-6}$ in the second image where t is the rescaled dimensionless time. Parameters in this simulation are the same as those in figure 10 and the x-axis in each image runs from 0 to 0.1 cm.

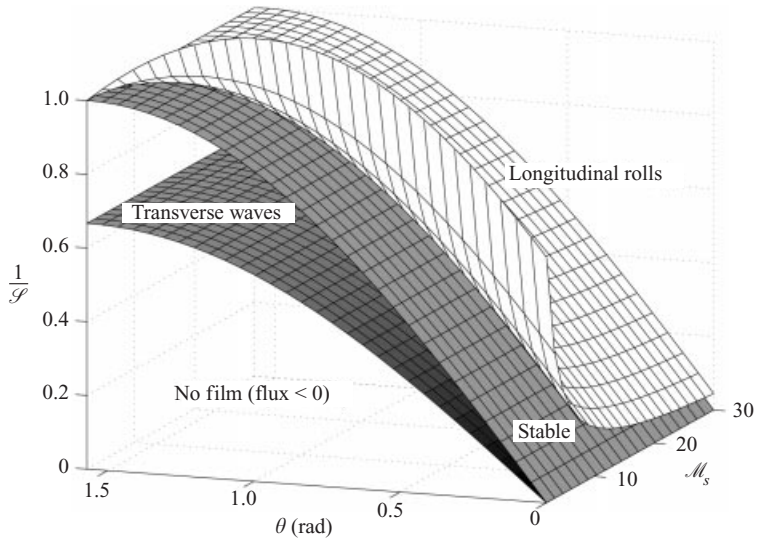

FIGURE 14. Stability diagram illustrating the transitions between stable states, transverse waves and longitudinal rolls. Recall that θ is the plate inclination angle, $1/\mathscr{S} = \tau/(\rho g H)$ and $\mathscr{M}_s = \tau H^2/(D\mu)$. The lower surface is defined by $1/\mathscr{S} = (2/3)\sin\theta$, the next by $1/\mathscr{S} = \sin\theta$ and the top surface $1/\mathscr{S} = 4\cos\theta/(3\mathscr{M}_s) + \sin\theta$. As θ approaches $\pi/2$ or as the Marangoni number becomes large, the top surface asymptotes to $1/\mathscr{S} = \sin\theta$ and the region of stability between transverse waves and longitudinal rolls vanishes. Note that the region that supports transverse waves increases with θ; thus we are more likely to observe this instability when the plate is nearly vertical.

is critical both in aligning the convection rolls and in establishing a convectively unstable concentration profile across the thin film.

Figure 14 summarizes the results of our theoretical study, which yields criteria for convection within a climbing film. The criterion for transverse waves, as deduced

from Smith & Davis (1983*b*), has been included for the sake of completeness. At a particular inclination angle and Marangoni number, increasing the surface stress leads one through three distinct regimes characterized by transverse waves, stable planar flow, and longitudinal convection rolls with associated surface deformations. Note that the parameter range characterized by transverse waves is greatly diminished at low θ, in accord with experimental observations. For any non-zero Marangoni number, there is a critical surface stress, defined by (4.32), capable of supporting longitudinal rolls in the thin film. This critical value is greatly diminished at large Marangoni numbers, where the regime of film stability becomes vanishingly small. Finally, it is instructive to note that the stability criterion of Smith & Davis (1983*a*) for a flat horizontal interface at $g = 0$ and with $\mathscr{P}r \to \infty$ predicts that as $1/\mathscr{S} \to \infty$, the system will be stable for all $\mathscr{M}_s < 15$. Our diagram clearly indicates the possibility of instability for all $\mathscr{M}_s$ (at sufficiently large $1/\mathscr{S}$), and thereby illustrates the destabilizing influence of the deformable interface.

Quantitative confirmation of the theoretical predictions would require an experimental study which allowed simultaneous measurement of film thickness and concentration profiles. While such a study has not yet been undertaken, there is qualitative experimental agreement with a number of predicted trends; specifically, the prevalence of transverse waves only at high inclination angles, and the diminished zone of flow stability at high Marangoni number. We see from table 4 that our experiments are characterized by large $\mathscr{M}_s$ and moderate $\mathscr{S}$; consequently, the prevalence of the longitudinal rolls in our experiments at small θ is consistent with our theoretical model.

6.1. *Three-dimensional effects*

The laboratory flows exhibit behaviour which is markedly three-dimensional, but which nevertheless may be understood in the context of our simplified two-dimensional model. In accordance with the observations of Vuilleumier *et al.* (1995), we expect both film thickness and surface stress to decrease slowly with distance from the meniscus; consequently, the shear Marangoni number must decrease with distance from the meniscus. In advancing up the plate, one expects to move from a region marked by the most vigorous nonlinear convection near the meniscus, through a region characterized by weakly supercritical convection, to a subcritical region in which convection is entirely absent. This progression roughly corresponds to that observed in advancing from the ridge region into the fine structure and beyond. We note however the potential importance of capillary pressure in the meniscus region where the ridges are most pronounced. Another clear manifestation of the flow's three-dimensionality was the emergence of surface waves only in the upper extremities of nearly vertical films: only at sufficient distance from the meniscus was the surface stress diminished to the extent that the criterion for transverse waves (4.38) was satisfied.

Directly after their formation, the ridges were the principal conduits for flow up the plane; however, the ridges would typically grow in both vertical and horizontal extent until their surface flow stopped and then reversed. This behaviour, which we refer to as 'slumping', is another manifestation of the three-dimensionality of the flow, but may again be simply understood in terms of our theoretical model. Specifically, the ridges can only grow to a critical height $H_{\max} = 3\tau/(2\rho g \sin\theta)$: for $H > H_{\max}$, the flow up the plane cannot be sustained. The resulting reversed or slumping flow will, according to the stability criterion (4.32) be stable to Marangoni convection.

When the plate inclination is small, the ducts assume a dendritic form (figure 6). In this case, the primary ducts play the role of the original slope: the trough-to-peak surface tension gradient supports an adjoining series of secondary ducts. The resulting

hierarchy of ducts gives the surface its dendritic pattern. Thomson (1855) released a small quantity of alcohol onto a thin layer of water, and noted the form of the thin central patch created by the radial surface divergence: '*the margin of the central patch is usually seen formed like as of leaves of a plant growing out all round*'. This dendritic structure may be readily reproduced in the laboratory, and may be understood as being the manifestation of analogous convective motions supported by a combination of evaporation and vertical shear associated with the radial Marangoni flow.

6.2. *Other possible manifestations of fine-scale convection*

The shear-alignment of Marangoni convection into longitudinal rolls arises in other situations involving surface tension gradients generated by either concentration, soluble surfactant or temperature gradients; for example, the fine convection rolls apparent in thin layers of coffee (Walker 1983), the ridges evident in the boundary of a film of water flowing down an incline (Hershey 1939), and the ridge structures evident in the meniscus region in a pan of hot cooking oil. When a candle is burning, a radial surface tension gradient is generated in the liquid wax owing to the temperature dependence of surface tension: vigorous convection is typically visible at the free surface, and is marked by fluid being driven outward along the free surface. When the flame is extinguished, the wax cools until it solidifies, and is often marked by radial ridges in the free surface which may be a remnant surface manifestation of Marangoni convection cells aligned by a radial flow.

The authors thank Michael Brenner and Harvey Greenspan for valuable discussions. This research was partially supported by the National Science Foundation under Award No. DMS-9705912.

Appendix. Solving the equations order by order

To lowest order, (4.14)–(4.22) become

$$u_{0zz} = 0, \quad v_{0zz} = \mathscr{S} \sin\theta, \quad p_{0z} = -\mathscr{S} \cos\theta, \tag{A 1a–c}$$

with boundary conditions

$$u_{0z} = 0, \quad v_{0z} = 1, \quad -p_0 = \mathscr{C} h_{xx} \quad \text{at} \quad z = h, \tag{A 2}$$

and $u = v = w = 0$ at $z = 0$. Applying these boundary conditions and integrating (A 1a) and (A 1b) twice and (A 1c) once in z (recall that h is not a function of z), we obtain the lowest-order solutions (4.25). Using these zeroth-order solutions, the next-order equations can be written as:

$$u_{1zz} = \mathscr{S} h_x \cos\theta - \mathscr{C} h_{xxx}, \quad v_{1zz} = 0, \quad p_{1z} = 0, \tag{A 3a–c}$$

with boundary conditions

$$u_{1z} = \mathscr{M}_s \left(\tfrac{1}{6}h^3 - \tfrac{1}{8}h^4 \mathscr{S} \sin\theta\right)_x, \quad v_{1z} = 0, \quad -p_1 = (y - c_0) h_{xx} \quad \text{at} \quad z = h, \tag{A 4}$$

and $u = v = w = 0$ at $z = 0$. Integrating in z gives the $O(\epsilon)$ velocities and pressures in (4.26).

REFERENCES

Bénard, H. 1900 *Rev. Gen. Sci. Pures Appl. Bull. Assoc. Franc. Avan. Sci.* **11**, 1261.

Bénard, H. 1927 Sur les tourbillons cellulaires et la théorie de Rayleigh. *Compt. Rendue* **185**.

Berg, J. C., Acrivos, A. & Boudart, M. 1966 Evaporative convection. *Adv. Chem. Engng* **6**, 61–123.

Berg, J. C., Boudart, M. & Acrivos, A. 1966 Natural convection in pools of evaporating liquids. *J. Fluid Mech.* **24**, 721–735.

Block, M. J. 1956 Surface tension as the cause of Bénard cells and surface deformation in a liquid film. *Nature* **178**, 650–651.

Burelbach, J. P., Bankoff, S. G. & Davis, S. H. 1988 Nonlinear stability of evaporating/condensing liquid films. *J. Fluid Mech.* **195**, 463–494.

Carey, V. P. 1992 *Liquid-Vapor Phase-Change Phenomena*. Taylor & Francis.

Chai, A.-T. & Zhang, N. 1998 Experimental study of Marangoni–Bénard convection in a liquid layer induced by evaporation. *Expl Heat Transfer* **11**, 187–205.

Davis, S. H. 1987 Thermocapillary instabilities. *Ann. Rev. Fluid Mech.* **19**, 403–435.

Fanton, X. & Cazabat, A. M. 1998 Spreading and instabilities induced by a solutal Marangoni effect. *Langmuir* **14**, 2554–2561.

Fournier, J. B. & Cazabat, A. M. 1992 Tears of wine. *Europhys. Lett.* **20**, 517.

Gumerman, R. J. & Homsy, G. M. 1974 Convective instabilities in concurrent two phase flow: Part i. Linear stability. *AIChE J.* **20**, 981–988.

Hershey, A. V. 1939 Ridges in a liquid surface due to the temperature dependence of surface tension. *Phys. Rev.* **56**, 204.

Koschmieder, E. L. 1967 On convection under an air surface. *J. Fluid Mech.* **30**, 9–15.

Lide, D. R. (Ed.) 1974 *Handbook of Chemistry and Physics: 72nd Edition 1991–1992*. CRC Press.

Marangoni, C. 1865 On the expansion of a drop of liquid floating on the surface of another liquid. Tipographia dei fratelli Fusi, Pavia.

Myers, T. G. 1998 Thin films with high surface tension. *SIAM Rev.* **40**, 441–462.

Nield, D. A. 1964 Surface tension and buoyancy effects in cellular convection. *J. Fluid Mech.* **19**, 341–352.

Oron, A., Davis, S. H. & Bankoff, S. G. 1997 Long-scale evolution of thin liquid films. *Rev. Mod. Phys.* **69**, 931–980.

Oron, A. & Rosenau, P. 1994 On a nonlinear thermocapillary effect in thin liquid layers. *J. Fluid Mech.* **273**, 316–374.

Pearson, J. R. A. 1958 On convection cells induced by surface tension. *J. Fluid Mech.* **4**, 489–500.

Rayleigh, L. 1916 On convective currents in a horizontal layer of fluid when the higher temperature is on the under side. *Phil. Mag.* **32**, 529–546.

Richter, F. M. & Parsons, B. 1975 On the interaction of two scales of convection in the mantle. *J. Geophys. Res.* **80**, 2529–2541.

Ross, S. & Becher, P. 1992 The history of the spreading coefficient. *J. Colloid Interface Sci.* **149**, 575–579.

de Ryck, A. 1999 Instability of a meniscus due to surface tension gradient-driven flow. *J. Colloid Interface Sci.* **209**, 10–15.

Scriven, L. E. & Sternling, C. V. 1960 The Marangoni effects. *Nature* **187**, 186–188.

Scriven, L. E. & Sternling, C. V. 1964 On cellular convection driven by surface-tension gradients: effects of mean surface tension and surface viscosity. *J. Fluid Mech.* **19**, 321–340.

Smith, K. A. 1966 On convective instability induced by surface-tension gradients. *J. Fluid Mech.* **24**, 401–414.

Smith, M. K. & Davis, S. H. 1983*a* Instabilities of dynamic thermocapillary liquid layers. Part 1. Convective instablities. *J. Fluid Mech.* **132**, 119–144.

Smith, M. K. & Davis, S. H. 1983*b* Instabilities of dynamic thermocapillary liquid layers. Part 2. Surface-wave instabilities. *J. Fluid Mech.* **132**, 145–162.

Thomson, J. 1855 On certain curious motions observable at the surfaces of wine and other alcoholic liquors. *Phil. Mag.* **10**, 330.

Vidal, A. & Acrivos, A. 1968 Effect of nonlinear temperature profiles on the onset of convection driven by surface tension gradients. *I&EC Fund.* **7**, 53–58.

Volkoviski, V. 1935 Sur les tourbillons en festons. *Compt. Rendue* **200**, 1285.

Vuilleumier, R., Ego, V., Neltner, L. & Cazabat, A. M. 1995 Tears of wine: The stationary state. *Langmuir* **11**, 4117–4121.

Walker, J. 1983 What causes the 'tears' that form on the inside of a glass of wine? *Sci. Am.* **234**, 162–169.

Yang, W.-J. 1999 The third type of Bénard convection induced by evaporation. In *Fluid Dynamics at Interfaces* (ed. W. Shyy & R. Narayanan), pp. 31–42. Cambridge University Press.